J. Fluid Mech. (2001), *vol.* 435, *pp.* 191–215. Printed in the United Kingdom

Observations of solitary wave dynamics of film flows

By M. VLACHOGIANNIS AND V. BONTOZOGLOU

Department of Mechanical and Industrial Engineering, University of Thessaly, GR-38334 Volos, Greece

(Received 20 April 2000 and in revised form 10 November 2000)

Experimental results are reported on non-stationary evolution and interactions of waves forming on water and water–glycerol solution flowing along an inclined plane. A nonlinear wave generation process leads to a large number of solitary humps with a wide variety of sizes. A fluorescence imaging method is applied to capture the evolution of film height in space and time with accuracy of a few microns. Coalescence – the inelastic interaction of solitary waves resulting in a single hump – is found to proceed at a timescale correlated to the difference in height between the interacting waves. The correlation indicates that waves of similar height do not merge. Transient phenomena accompanying coalescence are reported. The front-running ripples recede during coalescence, only to reappear when the new hump recovers its teardrop shape. The tail of the resulting solitary wave develops an elevated substrate relative to the front, which decays exponentially in time; both observations about the tail confirm theoretical predictions. In experiments with water, the elevated back substrate is unstable, yielding to a tail oscillation with wavelength similar to that of the front-running ripples. This instability plays a key role in two complex interaction phenomena observed: the nucleation of a new crest between two interacting solitary humps and the splitting of a large hump (that has grown through multiple coalescence events) into solitary waves of similar size.

1. Introduction

Recent progress in the theory of nonlinear dynamics of falling film flows has centred on the existence and properties of coherent structures, or dissipative solitary waves. A series of simplified equations have been developed over the last three decades (Benney 1966; Shkadov 1967; Prokopiou, Cheng & Chang 1991; Yu *et al.* 1995; Lee & Mei 1996; Nguyen & Balakotaiah 2000), resulting from the full Navier–Stokes equations by a long-wave approximation and by various order-of-magnitude assumptions for the pertinent dimensionless Reynolds and Weber numbers Re and We. Intensive analytical and numerical scrutiny of these equations, based on dynamical systems techniques, has revealed multiple families of stationary solutions bifurcating from the primary instability of the flat film (Demekhin, Tokarev & Shkadov 1991; Trifonov & Tsvelodub 1991; Tsvelodub & Trifonov 1992; Chang, Demekhin & Kopelevich 1993; Chang 1994; Lee & Mei 1996). Few numerical simulations of the full Navier–Stokes equations have been undertaken (Bach & Villadsen 1984; Kheshgi & Scriven 1987; Ho & Patera 1990; Malamataris & Papanastasiou 1991; Salamon, Armstrong & Brown 1994) and all are restricted to relatively small Re. Therefore, the limits of validity of the approximate equations are still a matter of active research.

On the other hand, detailed experimental records of solitary wave dynamics in film flows are not very numerous. The pioneering work of Kapitza & Kapitza (1949), as well as later contributions (Stainthorp & Allen 1965; Jones & Whitaker 1966; Krantz & Goren 1971; Pearson & Whitaker 1977) mainly deal with the wavelength and speed of small-amplitude waves in the inception region. Alekseenko, Nakoryakov & Pokusaev (1985) have measured wave growth rates and compared them with the predictions of linear stability theory. They also documented the relation between height and speed of solitary waves and even anticipated some of the modern results on wave–wave interaction. Chu & Dukler (1974) and Yu *et al.* (1995) have measured the downstream evolution of a falling film towards a highly irregular state.

A series of papers by Gollub and coworkers (Liu, Paul & Gollub 1993; Liu & Gollob 1994) has decisively confirmed the predictions of linear stability theory, as well as the role of subharmonic and sideband instabilities in initiating the transition from noise-sustained, small-scale disturbances (of the length of the linearly most unstable wave) to large-scale coherent structures. In addition, Liu & Gollub (1994) have studied the dynamics of two-dimensional solitary waves experimentally and – among other finding – have clearly demonstrated the interaction between solitary waves leading to coalescence.

Solitary wave interaction is a central topic of nonlinear theories and has been considered in various contexts. Non-dissipative systems – the Korteweg–de Vries equation being a prime example – are predicted to exhibit elastic collisions, whereby humps of different size pass through one another preserving their original features with only a change in phase (Mei 1989). Numerical simulations of dissipative systems indicate that coalescence, i.e. totally inelastic collisions like the ones observed by Liu & Gollub (1994), take place under certain circumstances.

However, coalescence is only one of the possible simulation outcomes. Chang, Demekhin & Kalaidin (1995), studying analytically and numerically the vertical falling film flow on a flat plate, have predicted the formation of bounded pairs and double-hump pulses as a result of the balance between attractive and repulsive interactions of approaching solitary waves. Kerchman & Frenkel (1994), investigating axisymmetric film flow over a vertical fibre, have numerically computed almost elastic collisions between drops of unequal size. However, Liu & Gollub (1994) have observed nothing but coalescence interactions between solitary waves; thus, the other predicted events appear as yet unconfirmed by experiment.

Chang *et al.* (1995) have developed a detailed theory of solitary wave dynamics, based on the interaction of the tail of a preceding hump with the front-running ripples of the following hump. Their theory predicts that a coalescence event results in the transient formation of an excited hump, which is higher than the typical solitary wave for the specific flow conditions and possesses a hydraulic jump at the tail. While moving downstream, the exited hump gradually decays by releasing fluid from the hydraulic jump. Both the wave height and the back substrate level tend asymptotically to the normal values, unless another solitary wave is encountered and a new coalescence takes place. The ingredients of this predicted mechanism appear not to have been confirmed experimentally.

Though falling film flow has emerged as a prominent paradigm for testing nonlinear dynamic system theories, a limitation has been noted: more specifically, the main difficulty in exhaustively studying solitary wave dynamics through falling film experiments lies in the rapid development of three-dimensional instabilities (Chang *et al.* 1994; Liu, Schneider & Gollub 1995). These secondary instabilities typically wreck the possibility of recording persistent interactions of two-dimensional structures (Balmforth 1995).

With respect to the above, the goal of the present work is to create a large number of two-dimensional solitary waves over a short fetch by a nonlinear generation process, and thus to be able to observe rich interactions. This is accomplished by introducing periodic flow pulses, similarly to the procedure adopted by Alekseenko *et al.* (1985). The main difference from their work is that the film is now unstable even at the base flow rate; as a result, more intense interactions develop over a short fetch.

2. Experimental method

2.1. *Experimental set-up*

In this section, we first describe the experimental apparatus for producing and perturbing the film flow. We then describe the fluorescence imaging system, which is used to obtain quantitative measurements of the film thickness as a function of time and space. Finally, we discuss the image processing analysis, which involves extensive use of appropriate software.

The experimental apparatus is shown schematically in figure 1. An elevated overflow tank is used to maintain a constant liquid head. Flow rate is varied by a manually operated valve, and is determined by measuring the volume of liquid flowing out of the channel over a known period of time. All experimental measurements are made at steady state, i.e. after a constant flow rate has been achieved. The fluid is stored in the collection tank (see figure 1), from where it is pumped to the overhead tank. The collection tank has no stiff connections with other parts of the experimental device, and the pump is submerged into the water to minimize transmission of vibrations.

From the overhead tank, the fluid is directed by three elastic tubes to the distributor head. A timer-controlled on/off electro-valve is located at a bypass exit below the distributor head, in order to disturb the film flow by blocking the bypass stream and thus creating an extra flow surge at the channel entrance. The above perturbation system (timer, electro-valve) can accommodate disturbances with a range of frequencies from 0.1 to 1 Hz. The extent of each disturbance depends on the time duration of the flow surge, which is varied in the range 0.2–2.0 s. An alternative perturbation system used involves an oscillating stopcock, which blocks the exit of the bypass stream to the collection tank. The stopcock is driven by a variable-frequency motor spanning a frequency range of 1–10 Hz.

The main channel is made of Plexiglas and has length 800 mm, width 250 mm and height 20 mm. The entire apparatus is mounted on rubber sheet to reduce the influence of any vibrations. The channel can operate at an inclination angle φ ranging from 0° to 60°. However, the range used in the present work is 2°–7°. This allows the amplification rate of waves to be adjusted in connection with the imposed disturbance, so that meaningful observations are made in the available channel length.

The liquids used in the experiments are pure water and a 28% by weight solution of glycerol in water. Two-dimensional waves are more stable against three-dimensional disturbances in the water–glycerol solution, permitting observations at higher Reynolds numbers or steeper inclination angles. The liquid is changed for each set of experiments and the viscosity of water–glycerol solutions is determined indirectly by measuring the refractive index with a refractometer. Physical properties of the water–glycerol solution at 25 °C (working temperature, ± 1 °C) are kinematic viscosity $\nu = 2.13 \times 10^{-6}\,\mathrm{m^2\,s^{-1}}$, surface tension $\sigma = 70 \pm 1 \times 10^{-3}\,\mathrm{N\,m^{-1}}$ and density $\rho = 1066.4\,\mathrm{kg\,m^{-3}}$. The surface tension of pure water is taken as $\sigma = 72 \pm 1 \times 10^{-3}\,\mathrm{N\,m^{-1}}$.

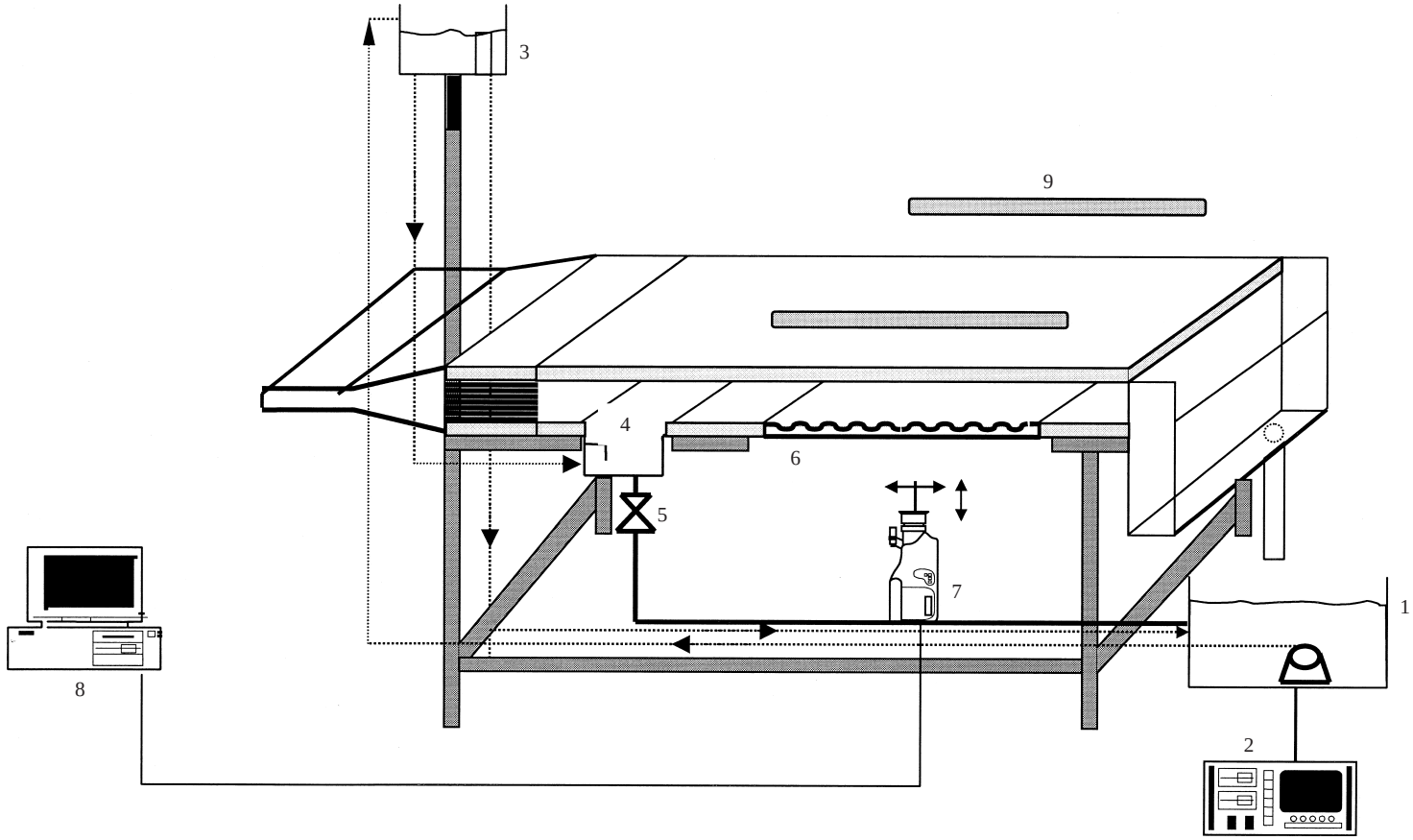

FIGURE 1. Sketch of the experimental apparatus: 1. collection tank; 2. current-voltage transformer; 3. overflow tank; 4. distributor head; 5. on/off electro valve; 6. removable test surface; 7. CCD camera Sony XC-77/77CE; 8. PC with frame grabber board; 9. UV light lamps.

The Kapitza number, $Ka = \sigma/\rho\, g^{1/3}\, v^{4/3}$, which characterizes the liquid that is used, is 3365 for water, and 1102 for the water–glycerol solution. The Reynolds number of the flow is defined as $Re = q/v = \langle u \rangle h_N/v$, where q is the volumetric flow rate per unit width, h_N is the Nusselt film thickness and $\langle u \rangle$ is the average streamwise velocity. The flow is also characterized by the We number, defined as $We = \sigma/\rho \langle u \rangle^2 h_N$. The use of two liquids with different viscosities offers some flexibility as noted above. However, the resulting variation in Kapitza number is too small to permit a detailed investigation of its effect.

2.2. *Fluorescence imaging method*

In order to describe the spatial and temporal dynamics for nonlinear waves, it is necessary to obtain space–time measurements. To achieve this, we use the fluorescence imaging method described by Liu *et al.* (1993). In our experiments, we dope the fluid with a small concentration, about 200–300 p.p.m. of dye (sodium salt of fluorescein; $C_{20}H_{10}O_5Na_2$), which fluoresces under ultraviolet light and which has been proved to leave the relevant physical properties of the liquid unaffected. The ultraviolet (UV) source consists of two high-intensity lamps (Philips, TL20/05), which are located above the lateral edges of the test surface at a specific distance from the film plane. The above parameters (dye, concentration of dye, ultraviolet source, distance from the film plane) are kept as close to constant as possible, with the calibration taking care of small variations.

A high-resolution CCD camera (Sony XC-77/77CE) and a monochrome frame grabber board (Data Translation DT3155) are used to acquire and digitize the flow images up to a maximum speed of 20 frames per second. A combination of two optical filters (green corrective, yellow subtractive) mounted on the camera assures that only light in the fluorescence wavelength range is recorded. Acquired images are digitized at 576×768 pixels with 8-bit of resolution and each frame corresponds to an $85\,\text{mm} \times 114\,\text{mm}$ window of channel area. To increase the grabbing speed, we store the images in the random access memory (RAM) by using commercial (HLImage++), as well as in-house software, and then we save them on the hard disk.

The light intensity in the image plane is found to vary linearly with the local film thickness. The relation between the fluorescence intensity $I(x, y, t)$ and the film thickness $h(x, y, t)$ is modelled by the expression

$$I(x, y, t) = a(x, y)\, h(x, y, t) + b(x, y). \tag{1}$$

The two linear coefficients vary with the (x, y) location because of non-uniformity of the UV light field; they also depend on the parameters mentioned above and on the kind of solution used. Thus, the calibration procedure produces independent a and b values for each pixel of the field of view. Calibration is based on the conclusion of linear stability theory – verified experimentally by Liu *et al.* (1993) – that the critical Reynolds number for growth of the most unstable disturbance is $Re_c = \frac{5}{6} \cot \varphi$, where φ is the inclination angle of the wall. Therefore, in the stable range of Reynolds numbers and inclination angles, the film thickness is equal to the Nusselt film thickness.

This assertion has also been confirmed by independent measurement of the film thickness by a contact needle and a displacement micrometer. The technique used involves imposition of a small voltage difference between the tip of the metallic needle and the liquid inside the channel, which is conducting. The needle is gradually lowered towards the surface of the stable film and, as soon as it touches the surface, the electric circuit closes and an alarm is activated. The absolute agreement between

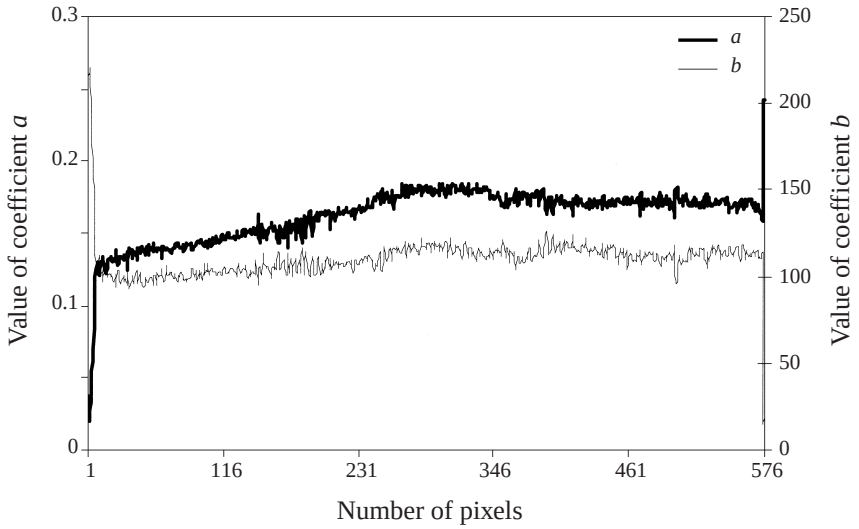

FIGURE 2. The two coefficients a, b for each pixel along a transverse line. A 28%wt water–glycerol solution is sued in this experiment.

measurements and predictions based on Nusselt theory, serves as a consistency check of the channel levelling and of the accuracy of the imposed flow rate and inclination angle.

Data taken in the above stable range are used to derive the correlation between fluorescent light intensity and the known film thickness. The linear relation (1) is always found to be satisfactory (accurate to within 2–5% for film thickness in the range of 0.2–2.0 mm) and a and b are obtained by a best fit. As for the variation of a and b over the image, an indicative example of the pixel values on a line profile in the transverse direction is shown in figure 2. A high-frequency error, due to digitization noise, appears and is eliminated by applying a convolution filter at the incoming images. The matrix of a and b values is used for the specific experimental run, and the calibration is repeated with every new set of experiments because the UV light intensity gradually fades with time.

2.3. *Image analysis*

Image processing is accomplished by using the MATLAB software. Each image, which corresponds to a snapshot of the field of view at a specific time instant, is converted into a two-dimensional matrix (576×768 elements). By treating images as matrices, we add flexibility in analysing and displaying data. The usual forms of presentation are instantaneous profile scans in the streamwise or the transverse direction and time series at one or multiple locations.

In figure 3, an example of the fluorescence imaging method is depicted with three consecutive images and their streamwise line profiles. What is actually shown is the progression of a large solitary wave. All the profiles are taken at mid-distance from the sides of the channel. A slight curvature of the wavefronts is observed in the 8 cm-wide images (see, for example, figure 3), which results from the influence of the lateral boundaries. Liu *et al.* (1993), have confirmed that curvature does not affect quantitative agreement between linear stability theory and experiment. More importantly, the interactions between solitary waves to be described next are always two-dimensional, as has been repeatedly checked by sampling off the channel

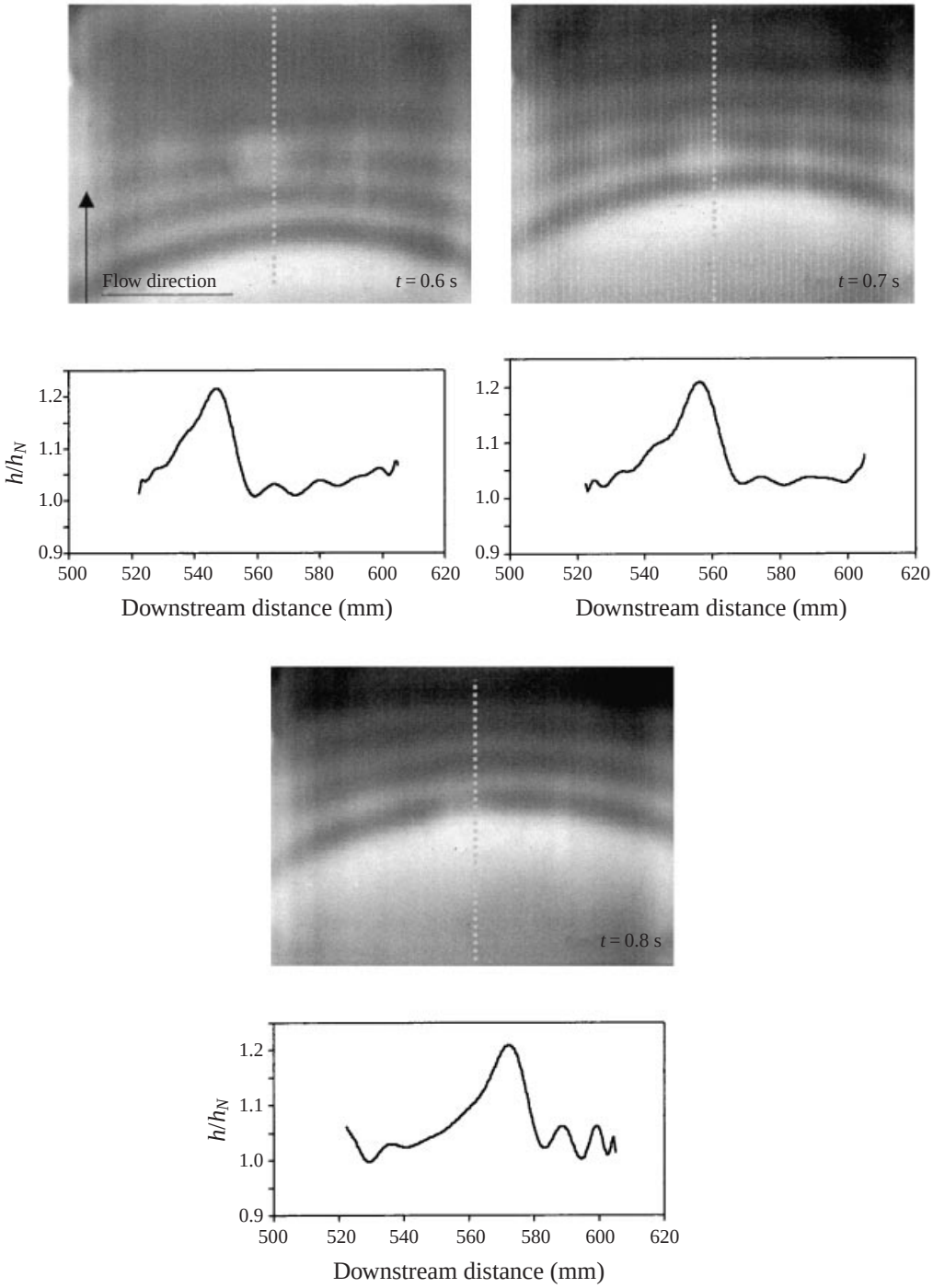

FIGURE 3. An example of consecutive fluorescence images and the corresponding line profiles $h(x)$ for water film at $\varphi = 5°$, $Re = 27$ and $Ka = 3365$.

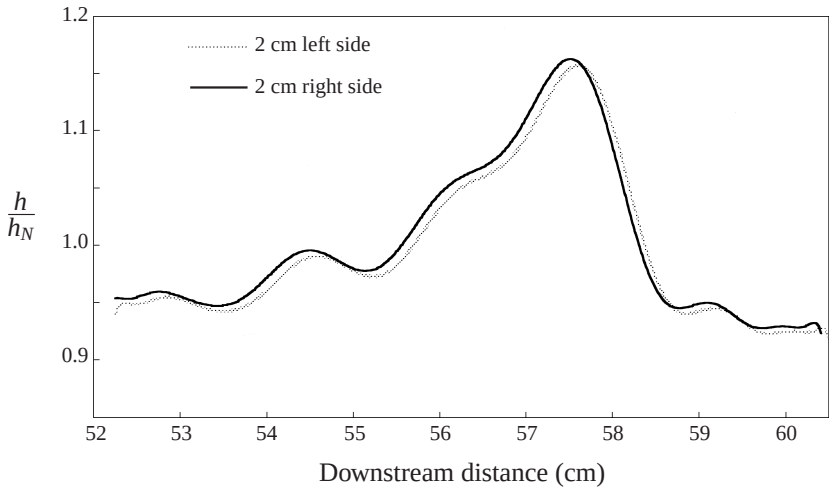

FIGURE 4. Two streamwise line profiles displaced symmetrically a distance 2 cm from the centreline. The inclination angle is $\varphi = 4^\circ$ and aqueous solution of glycerol (28%wt) is used.

centreline. An example of such a check is shown in figure 4, where streamwise line profiles at two locations, symmetric about the centreline, are plotted. The distance between the two line profiles is 4 cm – or 2 cm from the centreline – and quantitative agreement is evident indicating that the waves are two-dimensional.

3. Outline of experimental realization

3.1. *Generation of series of solitary waves*

Before embarking into detailed documentation of specific events, it is necessary to describe in gross terms the experiment performed. A base film flow is established at a flow rate, q_0, above the limit of linear stability. The flow is periodically disturbed by blocking a bypass stream below the distributor head, and thus creating an extra flow surge, $\Delta q = q_1 - q_0$, at the channel entrance. The frequency of this disturbance is very low (typically $f = 0.1667$ Hz, or period $T = 6$ s), so that each surge evolves fairly independently, separated from the preceding and the following ones by stretches of substrate. The duration of a flow surge, t_1, is varied in the range 0.2–1.0 s.

The flow is characterized by Re defined in terms of the mean flow rate as

$$Re = \frac{\langle q \rangle}{\nu} = \frac{(t_0\, q_0 + t_1\, q_1)/(t_0 + t_1)}{\nu}, \tag{2}$$

where $t_0 = T - t_1$ is the duration of the base flow per period. Each surge results in an elevation of the liquid level at the entrance roughly in the order of 5% of the Nusselt film thickness corresponding to the base flow rate, q_0. Thus, an elongated but not very high hump is formed, that readily disintegrates into a series of waves, which evolve into solitary humps.

The downstream evolution of the inlet disturbance, in a representative run with glycerol solution at $Re = 37$, inclination angle $\varphi = 5^\circ$ and surge duration $t_1 = 1.0$ s, is shown in figure 5. What are actually depicted are film height time series at four points, located at distances 20, 150, 580 and 644 mm from the entrance to the channel. The general trend is that the inlet surge disintegrates into a series of large-amplitude

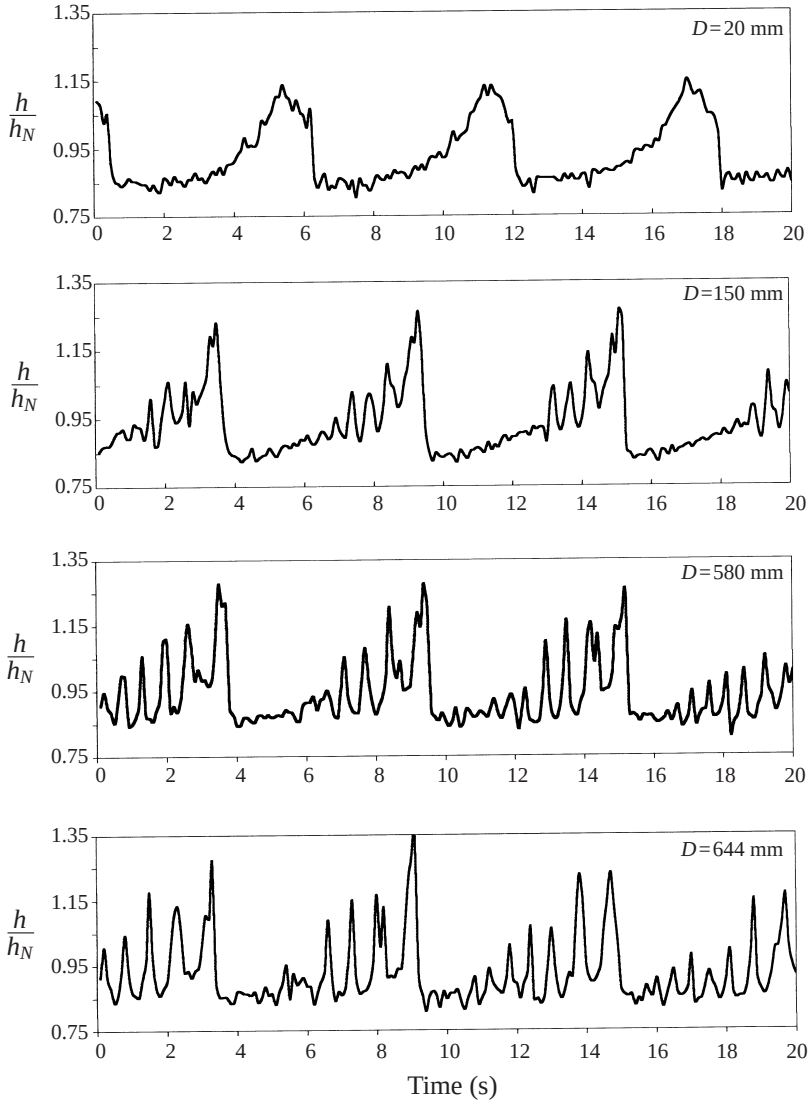

FIGURE 5. Spatial evolution of the normalized film thickness at four different downstream distances, for $Re = 37$, $\varphi = 5°$, $Ka = 1102$ and $t_1 = 1.0$ s. A series of fully developed solitary waves has formed at the last section of the channel.

waves, with the leading one usually being the highest (except in cases where specific interaction processes occur).

The effect of surge duration, liquid viscosity and Re number is shown in figure 6. Relatively few large waves are observed with the 28% glycerol solution, and their number gradually increases with the duration of the flow surge. This is evident from a comparison of the time traces in figures 6(a) and 6(b), which are taken at the same location – 644 mm from the entrance – and correspond to the same flow conditions except that $t_1 = 0.5$ s and 1.0 s, respectively. Water produces distinctively more solitary waves even with flow surges of smaller duration, as is demonstrated in figure 6(c) which corresponds to a $Re = 36$ and $t_1 = 0.5$ s. An increase in the

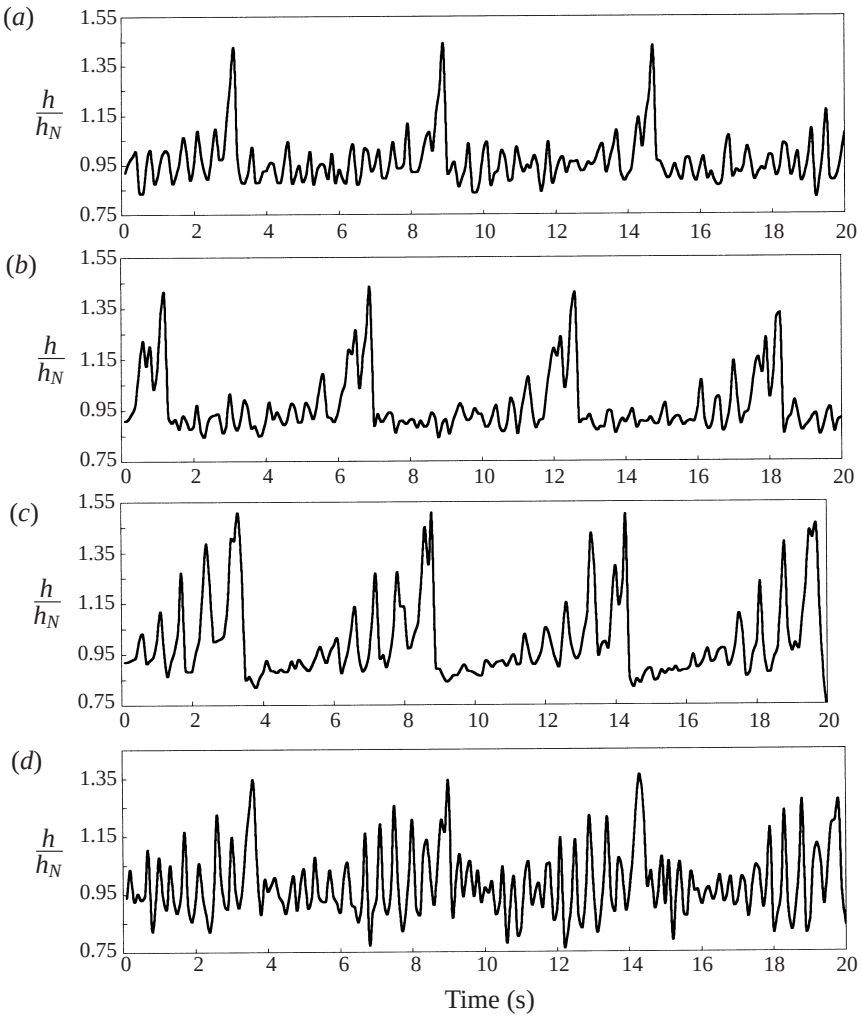

FIGURE 6. Comparison of time traces for different flow parameters at the same location (644 mm). The produced number and amplitude of solitary waves indicates the role of viscosity, inclination angle, Reynolds number and duration of the disturbance. (*a*) $Re = 52$, $\varphi = 3^\circ$, $Ka = 1102$, $t_1 = 0.5$ s; (*b*) $Re = 52$, $\varphi = 3^\circ$, $Ka = 1102$, $t_1 = 1.0$ s; (*c*) $Re = 36$, $\varphi = 4^\circ$, $Ka = 3365$, $t_1 = 0.5$ s; (*d*) $Re = 52$, $\varphi = 4^\circ$, $Ka = 3365$, $t_1 = 1.0$ s.

Re number and surge duration, with the other parameters kept constant, results as expected in a richer time signal (figure 6*d*).

Frequency power spectra of the time series of figure 6 are shown in figure 7. The first peak in figures 7(*a*)–7(*d*) always corresponds to the frequency ($f = 0.1667$ Hz) of the imposed flow disturbance. Superharmonics are evident and become stronger with increasing duration of the flow surge (compare figures 7*a* and 7*b*) and with increasing *Re*. The solitary waves, which result from the disintegration of the initial disturbance, gradually develop a local maximum in the intermediate frequencies of the power spectrum (see frequency range 1–1.5 Hz in figure 7*c* and 2–2.5 Hz in figure 7*d*).

A similar picture also emerges from wavenumber spectra, like the ones shown in figure 8 for water flow at inclination angle $\varphi = 5^\circ$ and *Re* 32 and 52. The broad background indicates a wide variety of waveforms, while the major peak corresponds

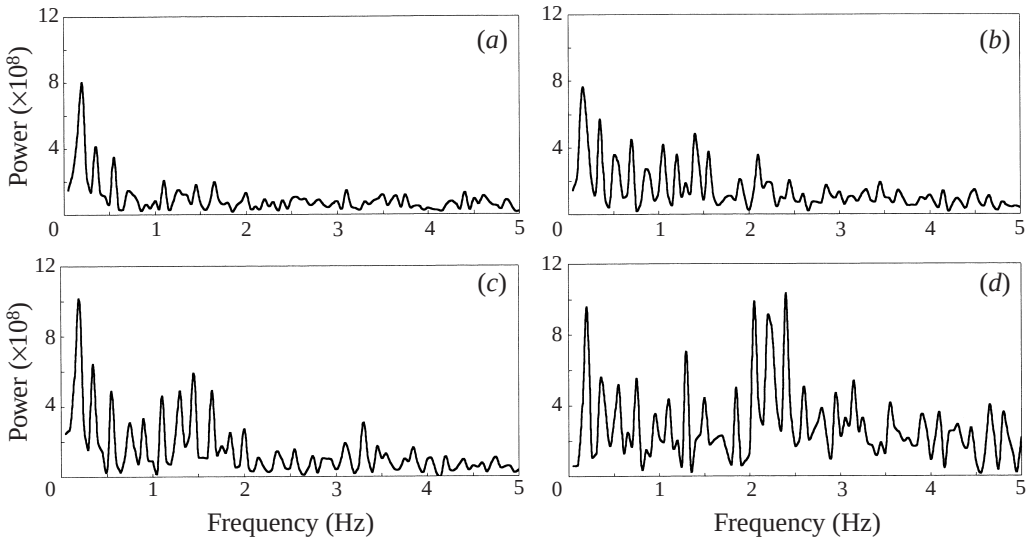

FIGURE 7. Frequency power spectra of the time-series of figure 6. The first peak always corresponds to the frequency (0.1667 Hz) of the imposed flow disturbance. (*a*) $Re = 52$, $\varphi = 3^\circ$, $Ka = 1102$, $t_1 = 0.5$ s; (*b*) $Re = 52$, $\varphi = 3^\circ$, $Ka = 1102$, $t_1 = 1.0$ s; (*c*) $Re = 36$, $\varphi = 4^\circ$, $Ka = 3365$, $t_1 = 0.5$ s, (*d*) $Re = 52$, $\varphi = 4^\circ$, $Ka = 3365$, $t_1 = 1.0$ s.

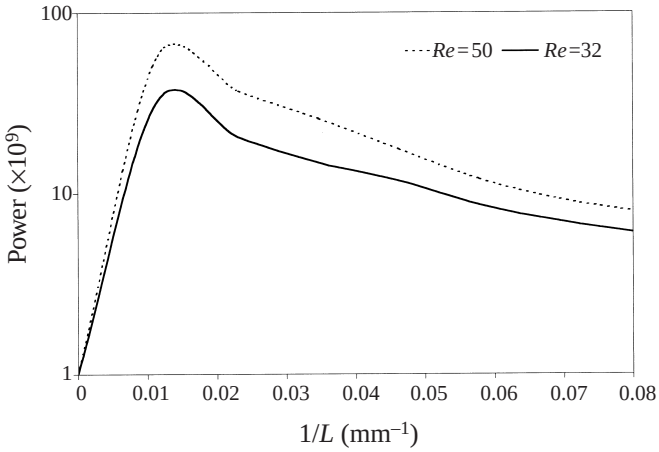

FIGURE 8. Wavenumber spectra for water flow at inclination angle $\varphi = 5^\circ$ and Reynolds numbers 32 and 52.

to wavelengths of the order of 5–10 cm, which are typical of the solitary humps created from the inlet flow surge.

For low-frequency forcing, as in the present experiment, quasi-stationary multi-peaked solitary waves are always observed, provided that three-dimensional instabilities have not grown significantly. The generation of these solitary waves, which are manifested in the above time series and power spectra, occurs through the simultaneous fast growth and phase locking of multiple harmonics of the initial nonlinear disturbance. Despite the limited length of our channel, we have taken care to assure that the documented interactions always involve solitary waves, which have emerged from their respective region of transient growth. For example, a comparison of fig-

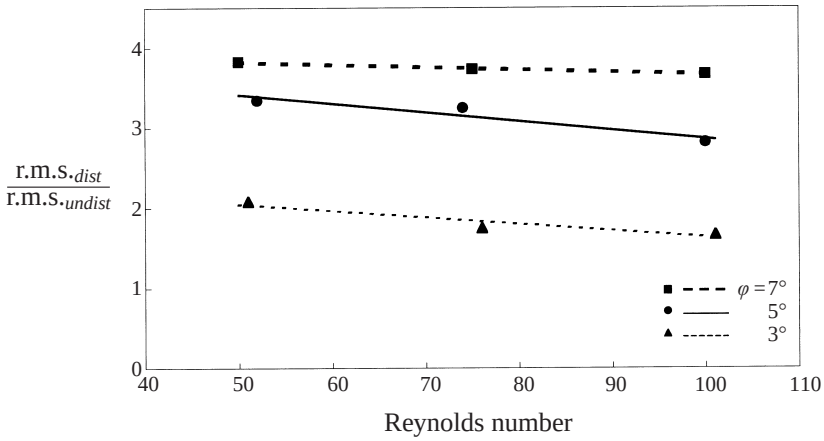

FIGURE 9. The ratio of r.m.s. values of appropriate sections of the time traces, for disturbed and undisturbed flow, as a function of the Reynolds number.

ures 5(*c*) and 5(*d*) indicates that the height of the solitary humps remains on the average constant in the last part of the channel. However, a true asymptotic state is actually never reached in the present experiments, because of the repeated wave–wave interactions (see, for example, the second wave in figure 5*d*). With a much longer channel, one would expect a spanwise instability to develop and render the small-scale structure three-dimensional, though the large-scale features have been reported to remain two-dimensional in an average sense (Liu & Gollub 1994).

Waves also grow from the rippled substrate between the major groups of solitary waves. These minor waves are lower than those developing directly from the flow surge, and in most cases the two can be easily distinguished. The role of subharmonic and sideband instabilities – as described by Liu & Gollub (1994) for an unforced film – is essential in the development of these new waves. However, their growth rate in the present experiment is significantly higher than that of their natural counterparts in a purely noise-sustained film.

The above assertion is demonstrated by performing experiments at the same *Re* and inclination angle but without flow surges. The results in figure 9 show the root-mean-square (r.m.s.) values of appropriate sections of the time traces, both with and without the entrance disturbance (excluding, in the case of forcing, the sections with major solitary waves), plotted as a function of *Re*. The enhanced evolution of substrate instabilities into minor solitary waves in the forced experiments is attributed to the high amplitude and the broad frequency spectrum of the inlet disturbance, which continuously radiates energy. The simultaneous existence of the major and minor waves permits the investigation of interactions between solitary humps of a great variety of sizes.

3.2. *Time-periodic nature of observed interactions*

The interactions between large solitary waves – formed by the disintegration of the entrance flow surge – and between these and the smaller ones developing on the substrate provide the basis for all the observations to be discussed in the rest of the paper. The interactions – as manifested by the instantaneous snapshots of the view window – seem at first sight of confusing complexity. However, up to moderate values of *Re* (of the order of 50), they are repeated with impressive faithfulness surge after surge. Upon systematic inspection, the high irregularity of the free-surface

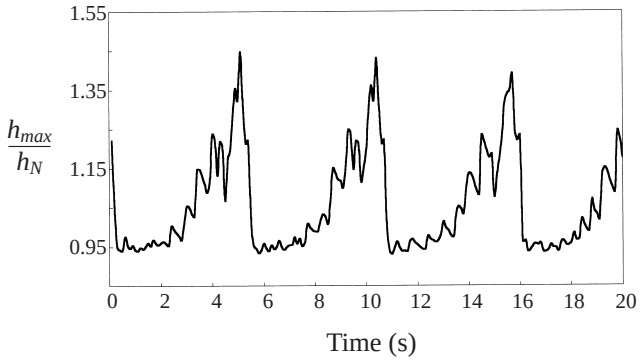

FIGURE 10. Evolution of maximum thickness $h_{\max}$ of the film residing in the 114 mm stretch of channel length under observation versus time, for the data of figure 6(*d*).

profiles appears to be caused (at least to some extent) by the continuous variation of the height of solitary humps as they interact in non-stationary manner with their surroundings.

The canonical nature of these spatial modulations is revealed by the following procedure. In each data frame, we identify the maximum film thickness – which evidently corresponds to the highest wave residing in the 114 mm stretch of channel length under observation – and plot it as a function of time. A similar transformation was used independently by Kerchman & Frenkel (1994), in the analysis of their computer data of solitary drops sliding down a vertical fibre.

The outcome of the above transformation for the highly complex time signal of figure 6(*d*) is shown in figure 10 and demonstrates an unexpected regularity, with almost identical sequences appearing in every surge. For a better interpretation of figure 10, note that each peak corresponds to a specific wave, which modulates in height as it moves through the view field. The steep changes occur when the larger wave leaves the view field and the next larger one provides the maximum thickness. We have observed that, not only is the static form of the transformed time signals similar in every period, but also the various interaction events to be described later (coalescence, splitting, wave nucleation) take place almost identically in each flow surge.

The combination of spatial irregularity within one period with faithful reproduction of the same events period after period is a striking feature of the flow. The observation is evidently related to the work of Carbone *et al.* (1996), who analysed spatio-temporal measurements of multi-peaked periodic waves by the bi-orthogonal decomposition technique. These investigators concluded that breaking of the symmetry of the original uniformly travelling, steady waveforms occurs, for low to medium *Re*, through purely spatial modulations.

4. Experimental results

4.1. *Occurrence and timing of coalescence events*

Coalescence, the inelastic interaction of a large solitary wave with a front running smaller one, has been documented experimentally by Liu & Gollub (1994) and predicted analytically and numerically by Chang *et al.* (1995). Our measurements also confirm that the leading, highest wave of each surge moves faster and always overtakes the preceding solitary waves, which have significantly smaller height. An

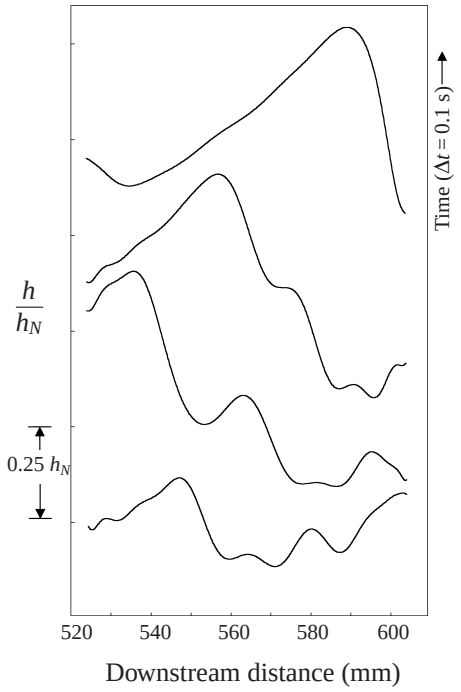

FIGURE 11. A coalescence event for $Re = 36$, $Ka = 3365$ and $\varphi = 5°$. The time interval between the wave profiles is 0.1 s and the amplitude scale is depicted on the left-hand side.

example of such an interaction is depicted in figure 11. The larger pulse, which emerges from the interaction, accelerates and possibly triggers further coalescence events. This phenomenon is completely different from the elastic interaction of two solitons in the KdV equation, where pulses merge and then separate unaffected apart from a phase change.

Examining the duration of the merging process provides an indication of the role of wave height difference in coalescence. Determination of the time lapse for merging to conclude is to some extent subjective. We choose to define the beginning of the event when a rippled substrate between the two waves ceases to exist and the end when there is a single major peak left. Following the scaling adopted by Chang *et al.* (1995), we non-dimensionalize the coalescence time with the characteristic time

$$t_0 = \frac{h_N \kappa}{\langle u \rangle} = \left(\frac{3\nu\, We}{g_x^2} \right)^{1/3} \tag{3}$$

where κ is a large number given by $\kappa^3 = \frac{1}{3}(Re\, We)$, which reflects the slow evolution character of the wave dynamics, and g_x is the component of gravity in the flow direction.

Based on the above definitions, we have examined a large number of coalescence events and have come to the conclusion that the dimensionless merging time depends mainly on the difference in height between the two waves. Results for all inclination angles examined and for both water and 28% glycerin solution are shown in figure 12. It is interesting to note that we have also included in the figure the coalescence event reported by Liu & Gollub (1994), which conforms to the trend depicted by our data. Furthermore, the exponential decline of the data in figure 12 supports the conclusion

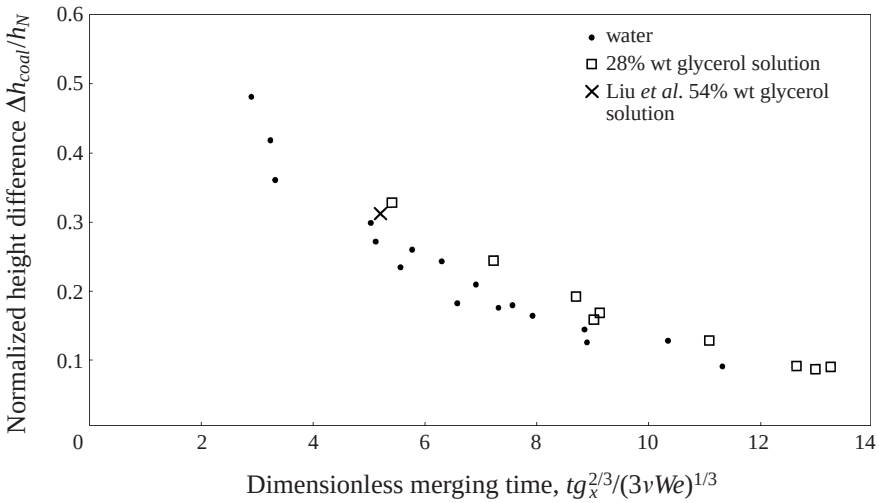

FIGURE 12. The difference in height between coalescing humps (normalized with the Nusselt film thickness) as a function of dimensionless merging time.

that coalescence does not take place below a minimum height difference of the order of $0.1\,h_N$.

There is one point that must be clarified with respect to the above arguments. Our view field permits observation for a typical time duration of 0.5–0.6 s. Therefore, it might be argued that coalescence still takes place but over a longer time interval, thus outside the observation window of the present experiment. However, all coalescence events observed demonstrate that, as soon as the two waves are close enough, drastic changes in the peak structure take place within a time-scale of the order of 0.1–0.2 s. On the contrary, we systematically observe sequences of similar waves, whose crests are close enough and which move through the view window without any activity. An example of such an observation is shown in figure 13, and may be compared with the sequence of figure 11. Actually, in figure 13 we witness a preceding wave gaining in height during the interaction with a larger, following hump. This is associated with the elevated back-substrate of the front wave, as will be discussed later.

4.2. *Transient phenomena accompanying coalescence*

Next, we proceed to discuss some small-scale characteristics of the coalescence events. Observation under the large discretization provided by the present experimental set-up reveals that there is change in the high-frequency content of solitary humps associated with the merging process. First, as soon as a single hump emerges, the bow waves in front of it temporarily recede, only to reappear a little later when the coalesced hump recovers the shape of a larger solitary wave. This temporary smoothing and rebuckling is shown in figure 14. The bow waves that appear ahead of the large solitary waves have wavelength λ_2, which agrees with the predictions of linear stability theory. This conclusion was documented by Nakoryakov, Pokusaev & Alekseenko (1976) and is confirmed by our results.

The speed of attainment of the final solitary shape after a merging event depends on the height difference of the interacting waves and on the physical properties of the liquid. For the more viscous glycerol solution and for low Reynolds numbers, the emerging wave approaches the solitary shape more slowly.

The role of the bow waves in retaining the stationary form of solitary waves has

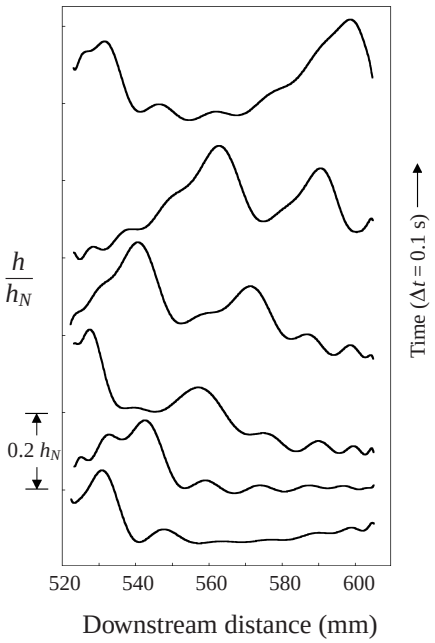

FIGURE 13. The interaction of a preceding wave with a larger following hump, which does not lead to coalescence ($Re = 27$, $\varphi = 5°$, $Ka = 3365$).

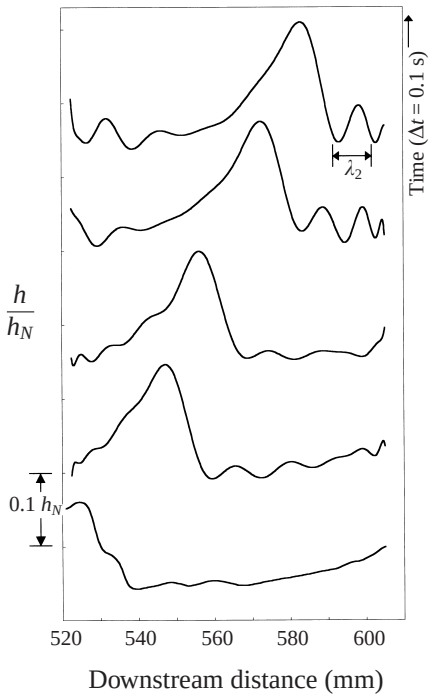

FIGURE 14. The temporary smoothing and rebuckling after a coalescence event ($Re = 27$, $Ka = 3365$, $\varphi = 5°$).

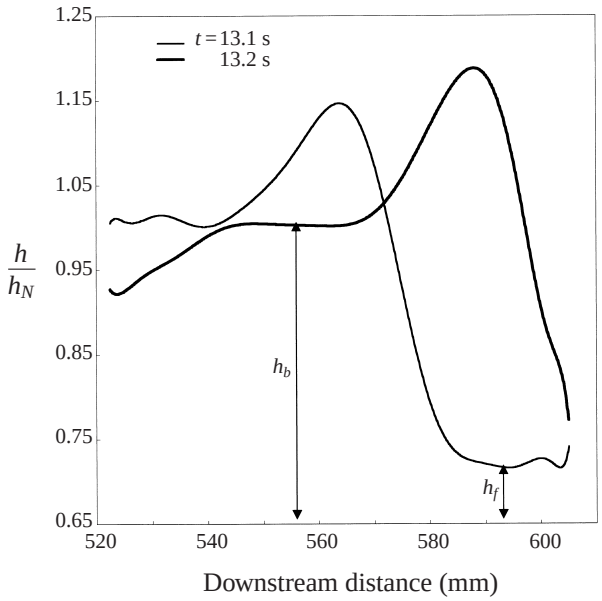

FIGURE 15. Documentation of an elevated back substrate for $Re = 75$, $Ka = 1102$ and $\varphi = 7°$.

been discussed by Chang *et al.* (1995), based on a lubrication analysis by Wilson & Jones (1983). In particular, these investigators argued that the ripples generate sufficient negative capillary pressure to drain fluid out from the crest, and in this way resist further steeping of the solitary hump imposed by the pull of gravity. The temporary disappearance of the front-running ripples after coalescence is thus explained by the time lag needed for the merged hump to attain the shape and speed of a solitary wave. When the hump further steepens by gravity, the ripples reappear. Viewed the other way around, our observation confirms experimentally the predicted role of bow waves. Temporary smoothing and rebuckling of the front substrate is evident in the coalescence event documented by Liu & Gollub (1994, their figure 12), but was not discussed by the authors.

The merging process is also accompanied by interesting phenomena at the back of the resulting solitary hump. Chang *et al.* (1995) have predicted that an excited solitary wave (the outcome of a coalescence event) is characterized by an elevated back substrate, h_b, which decays exponentially with time in synchrony with the wave height, h_m.

We have systematically confirmed the formation of excited waves with elevated back substrate in the experiments with the 28% glycerol solution and, less frequently and only for the smaller inclination angles, in the experiments with water (a description of phenomena unique to the water film will be given in the next section). A representative instant of the glycerol experiments is shown in figure 15, where a coalescence event has previously occurred (as witnessed by the temporarily smooth front substrate at $t = 13.1$ s) and the elevated back substrate is clearly depicted at the next instant ($t = 13.2$ s).

We have examined a large number of excited waves and recorded their substrate characteristics. Plotted in figure 16 is the dimensionless wave height, $(h_m - h_f)/h_f$, versus the dimensionless back-substrate thickness, $(h_b - h_f)/h_f$. The data have been taken at inclination angles 3°, 5° and 7°, and the three upper lines are the outcome of

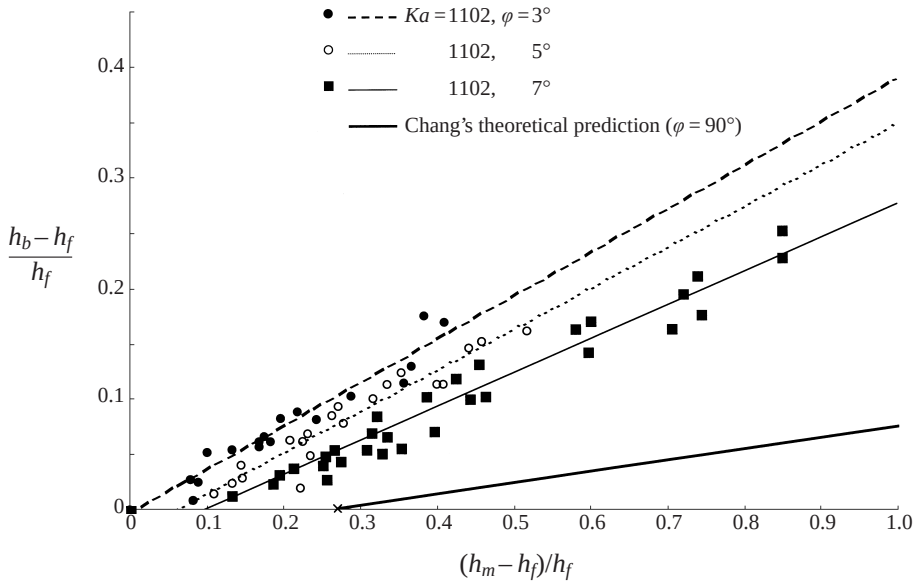

FIGURE 16. The dimensionless substrate difference $(h_b - h_f)/h_f$, versus the dimensionless wave height $(h_m - h_f)/h_f$ for excited humps resulting from coalescence events. Data for the glycerol solution at various Reynolds numbers.

a linear fit for each angle. Despite some scatter, there is a clear correlation between the two variables.

Chang *et al.* (1995), analysing vertical film flow, have devised a transformation of the single-parameter solitary wave family of the Kapitsa–Shkadov equation (parameterized by $\delta = Re^{11/9}/5\,Ka^{1/3}\,3^{7/9}$) into a family parameterized by $\chi = (h_b - h_f)/h_f$ for constant δ. Plotting their computed values for h_m and χ in a similar way, produces the lowest line in figure 16. Though, we do not have similar results for inclined flow, the trend in the linear fits is qualitatively consistent with these numerical data.

We have occasionally been able to follow the evolution in time of the back-substrate thickness of an excited wave. Relevant data are shown in figure 17, plotted in terms of dimensionless time, $t\,g_x^{2/3}/(3\nu\,We)^{1/3}$, and confirm the exponential decay predicted theoretically (Chang *et al.* 1995). The decay is best fitted by the expression $\chi(t) \sim \mathrm{e}^{-0.41t}$, with the exponent roughly an order of magnitude larger than numerically computed by Chang *et al.* (1995) for vertical film flow. The difference is qualitatively explained by the expected strong damping influence of the component of gravity normal to the wall. The latter is absent in vertical falling films but is very significant in the present experiments at small inclination angles. Viewed in dimensional time, the decay rate is found to be faster in water than in the glycerol solution. This finding is in accord with the general empirical observation that wave phenomena evolve slower in the more viscous solutions.

4.3. *The tail instability*

In experiments with water, the elevated back-substrate is observed rarely, and then it is highly unstable and yields to a tail oscillation with wavelength similar to that of the front-running bow waves. Such a sequence of events is shown in figure 18. Another example of evolution of the elevated back substrate into a tail modulation is provided

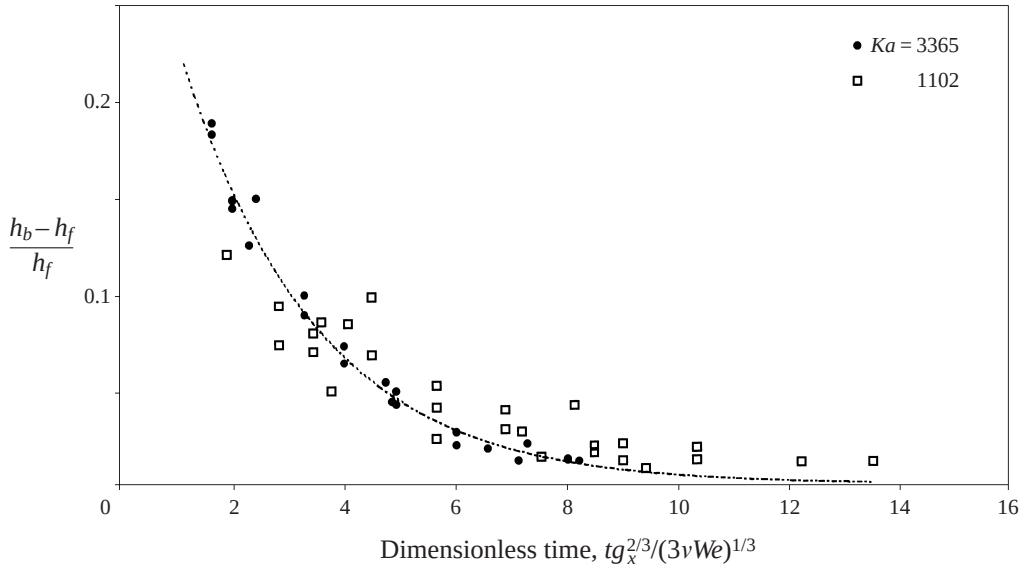

FIGURE 17. The decay of the elevated back substrate, in water and glycerol–water solutions, as a function of dimensionless time. – – –, exponential fit, $\chi^{(t)} = 0.35\,e^{-0.41t}$.

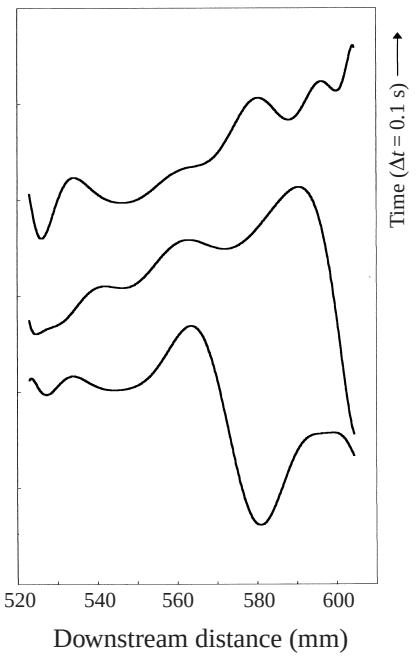

FIGURE 18. The evolution of the unstable elevated back-substrate, yielding to a tail modulation. Here, $Re = 27$, $Ka = 3365$ and $\varphi = 4°$.

by the front wave in figure 13. In most cases, however, completion of merging is directly accompanied by the transient development of this tail instability, without noticeable appearance of a flat elevated substrate. An example of this scenario is shown in figure 19 (or in the previously discussed figure 14) for a wave emerging from a coalescence event.

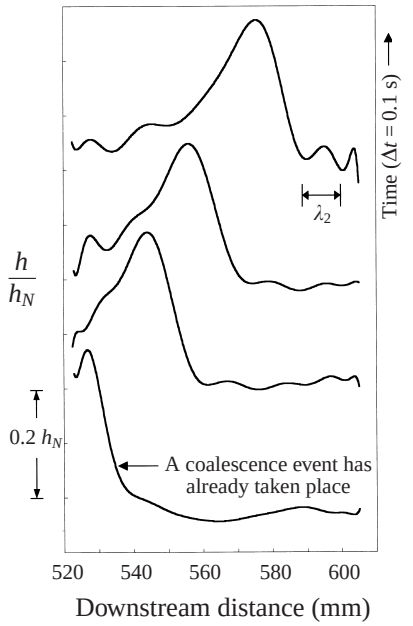

FIGURE 19. Demonstration of transient development of the tail instability. Here, $Re = 37$, $Ka = 3365$ and $\varphi = 4°$.

The above tail modulation, which accompanies solitary wave coalescence, appears not to have been discussed in the falling film literature. However, solitary waves with modulated tails have been recorded in experiments with sufficient spatial discretization (see for example Nguyen & Balakotaiah 2000, their figure 14). Re-adjustment of a solitary wave by creation of an oscillatory tail has been predicted for inviscid solitary waves of the Korteweg–de Vries equation. In particular, Gardner *et al.* (1967) demonstrated analytically that an initial hump disintegrates into a number of solitary waves followed by an oscillatory tail which is gradually left behind. A similar evolution has been predicted by Madsen & Mei (1969) for a solitary wave moving from a deeper to a shallower water layer.

As for the fate of the observed tail instability, when the solitary wave emerging from the coalescence event is isolated the oscillatory tail gradually lags behind the hump and eventually decays. However, if the excited wave is closely followed by another solitary wave, the tail modulation remains trapped between the two humps. It may temporarily reappear on the preceding wave tail, but eventually amplifies the major ripple of the following wave and nucleates a new hump between the two. Such an event is documented by the series of profiles in figure 20. In the same figure is clearly depicted the tail instability of the following wave which gradually decays because there is not a third wave accompanying it.

A variant of the wave nucleation triggered from the tail instability is observed with the first major hump of each flow surge. This hump grows continuously through repeated coalescence events with minor solitary waves. As a result, it develops a very strong tail instability, which grows faster near the crest and actually splits the wave into humps of comparable size. Such an event is depicted in figure 21.

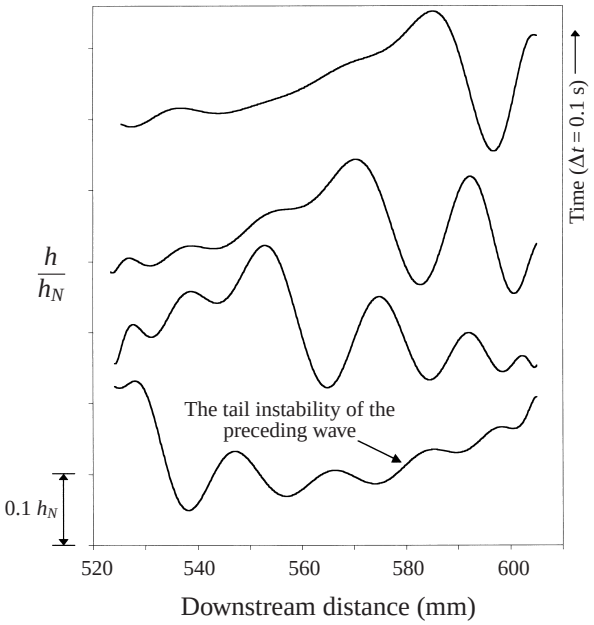

FIGURE 20. The nucleation of a new wave is plotted, as a result of the tail instability. The tail instability of the following solitary wave is isolated and the modulation eventually decays. Here, $Re = 50$, $Ka = 3365$ and $\varphi = 3°$.

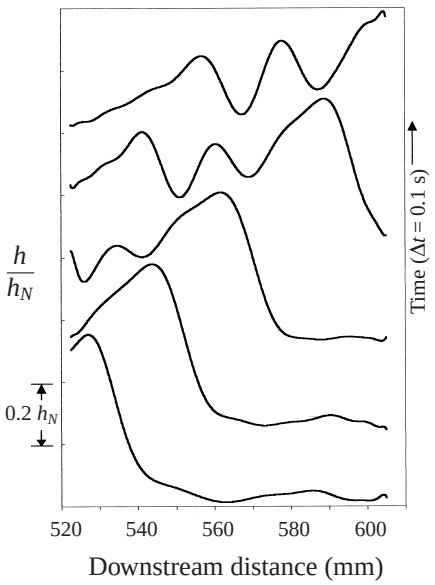

FIGURE 21. The splitting of a disproportionately large hump into a number of waves. Here, $Re = 75$, $Ka = 3365$ and $\varphi = 3°$.

5. Concluding remarks

Experiments were undertaken in an inclined channel flow, using a fluorescence imaging technique to measure the spatio-temporal evolution of the free surface. The

main goal has been to record and interpret the non-stationary evolution and the mutual interactions of solitary waves.

An elongated, low-frequency flow surge at the channel entrance has been used as a means of nonlinear wave triggering. The introduction of large flow surges (contrasted to the application of surface disturbances at constant flow rate) is not a widespread practice in the experimental study of film flows. However, in the present work, it proved an extremely efficient method of creating a large number of solitary waves over a short fetch. The wave evolution was found to exhibit spatial complexity coupled with temporal periodicity. In particular, all the complex events documented (coalescence, nucleation, splitting) were repeated regularly with each periodic flow surge.

We have systematically observed a large number of coalescence events and recorded their detailed characteristics. The time duration of the merging process was found to be inversely proportional to the height difference of the interacting humps, supporting the conclusion that humps of similar size do not coalesce but may form double-hump structures. To the best of our knowledge, this is the first experimental correlation of the above two parameters of solitary wave interaction. Thus, the data in figure 12 present qualitatively as well as quantitatively new results.

At the conclusion of each coalescence event, we have witnessed the temporary recession of the front-running ripples and the formation of an elevated back-substrate. The size of the substrate was found to scale with the height of the wave, and its decay with time was found to obey an exponential law. Our measurements of the characteristics and evolution of the elevated back-substrate provide the first experimental confirmation of the predictions of Chang *et al.* (1995). The comparison between theory and data is by necessity qualitative, as the former refers to a vertical film and the latter to small inclination angles.

In most experiments with water, the elevated substrate yielded to an instability producing an oscillatory tail. This tail was observed to lag behind an isolated hump and eventually decay. On the contrary, if the excited hump was followed closely by another solitary wave, the tail might be trapped in between and result in the nucleation of a new hump. This tail modulation appears not to have been previously noted in the falling-film literature, though it has long been known as an adjustment mechanism of inviscid solitons of the Korteweg–de Vries equation.

A qualitative description of wave–wave interactions – such as the above – and of the decay of excited solitary humps may be accomplished in terms of simple mass conservation arguments. Extending the mechanism described by Chang *et al.* (1995), we may view both the elevated back substrate and the outcome of its instability, the tail modulation, as effective means of draining liquid from the back of the tail. These mechanisms operate in parallel with the front-running ripples, which stabilize all solitary humps (normal or excited) by draining liquid out from the crest (as described in the first part of § 4.2).

In view of the above, a key parameter of wave–wave interaction seems to be the degree of excitation of the preceding wave, as represented by the elevation of its back substrate or the intensity of its tail oscillation. In particular, when the preceding wave is not excited it may be approached by a larger (i.e. faster) following wave. Then, the liquid draining out from the front of the second solitary wave raises the substrate between the two crests leading to the formation of a single hump.

On the contrary, a preceding excited wave resists coalescence with a bigger hump approaching from behind. If the difference in height is small, the two crests do not approach very closely. Liquid released from the tail of the preceding excited wave is then augmented by liquid drained from the front of the following wave and nucleation

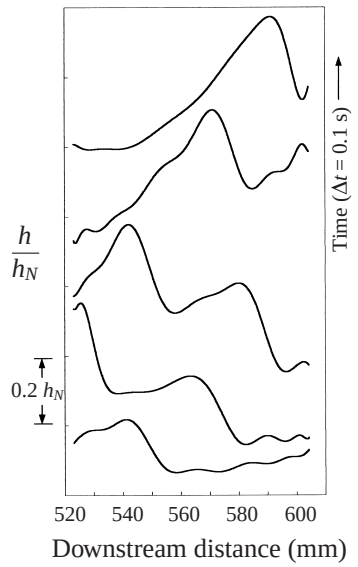

FIGURE 22. The interaction of a large solitary wave with a proceeding excited hump, which does not result in coalescence. Note the elevated back-substrate of the first wave, which gradually turns into a tail oscillation. Here, $Re = 50$, $Ka = 3365$ and $\varphi = 5°$.

of a new hump between the interacting waves may occur. Even when the following wave is much larger and sweeps the distance towards the first hump, it may be decelerated by the liquid draining from the tail of the excited preceding wave. The resulting structure then involves a quasi-stationary two-hump pulse. Such an event is recorded in figure 22 where, though the difference in height between the two waves is $\Delta h = 0.25\, h_N$, coalescence does not take place and the following hump remains unaltered in height and shape during more than 11 dimensionless time units.

Finally, it is noted that a more firm understanding of wave–wave interactions could result from time-dependent, two-dimensional simulations of film flow, based on the full Navier–Stokes equation of motion. Such results are now available and will be reported soon.

Professor Mark McCready of the University of Notre-Dame provided many useful suggestions for the design of the channel and also brought to our attention the paper by Liu *et al.* (1993). Professor Jerry Gollub of the University of Pennsylvania generously made available all the information on the fluorescence imaging method: we are grateful to both. Partial support to M.V. by a scholarship of the Greek National Fellowship Foundation is acknowledged.

REFERENCES

ALEKSEENKO, S. V., NAKORYAKOV, V. Y. & POKUSAEV, B. G. 1985 Wave formation on a vertical falling liquid film. *AIChE J.* **31**, 1446–1460.

BACH, P. & VILLADSEN, J. 1984 Simulation of the vertical flow of a thin wavy film using a finite element method. *Intl J. Heat Mass Transfer* **27**, 815–827.

BALMFORTH, N. J. 1995 Solitary waves and homoclinic orbits. *Ann. Rev. Fluid Mech.* **27**, 335–373.

BENNEY, D. J. 1966 Long waves on liquid films. *J. Math. Phys.* **45**, 150–155.

CARBONE, F., AUBRY, N., LIU, J., GOLLUB, J. P. & LIMA, R. 1996 Space-time description of the splitting and coalescence of wave fronts in film flows. *Physica* D **96**, 182–199.

Chang, H.-C. 1986 Traveling waves on fluid interfaces: normal form analysis of the Kuramoto–Sivashinsky equation. *Phys. Fluids* **29**, 3142–3147.

Chang, H.-C. 1989 Onset of nonlinear waves on falling films. *Phys. Fluids* A **1**, 1314–1327.

Chang, H.-C. 1994 Wave evolution on a falling film. *Ann. Rev. Fluid Mech.* **26**, 103–136.

Chang, H.-C., Cheng, M., Demekhin, E. A. & Kopelevich, D. I. 1994 Secondary and tertiary excitation of three-dimensional patterns on a falling film. *J. Fluid Mech.* **270**, 251–275.

Chang, H.-C., Demekhin, E. A. & Kalaidin, E. 1995 Interaction dynamics of solitary waves on a falling film. *J. Fluid Mech.* **294**, 123–154.

Chang, H.-C., Demekhin, E. A. & Kopelevich, D. I. 1993 Nonlinear evolution of waves on a falling film. *J. Fluid Mech.* **250**, 433–480.

Cheng, M. & Chang, H.-C. 1992 Subharmonics instabilities of finite-amplitude monochromatic waves. *Phys. Fluids* A **4**, 505–523.

Cheng, M. & Chang, H.-C. 1995 Competition between sideband and subharmonic secondary instability on a falling film. *Phys. Fluids* **7**, 34–54.

Chu, K. I. & Dukler, A. E. 1974 Statistical characteristics of thin wavy films. *AIChE J.* **20**, 695–706.

Demekhin, E. A., Tokarev, G. Yu. & Shkadov, V. Ya. 1991 Hierarchy of bifurcations of space-periodic structures in a nonlinear model of active dissipative media. *Physica* D **52**, 338–361.

Dukler, A. E. 1976 The wavy gas–liquid interface. *Chem. Engng Educ*. 108–120.

Gardner, C. S., Greene, J. M., Kruskal, M. D. & Miura, R. A. 1967 Method for solving the Korteweg–de Vries equation. *Phys. Rev. Lett*. **19**, 1095–1096.

Ho, L.-W. & Patera, A. T. 1990 A Legendre spectral element method for simulation of unsteady incompressible viscous free-surface flows. *Comput. Meth. Appl. Mech. Engng* **80**, 355–366.

Jones, L. O. & Whitaker, S. 1966 An experimental study of falling liquid films. *AIChE J.* **12**, 525–531.

Kapitza, P. L. & Kapitza, S. P. 1949 Wave flow of thin fluid layers of liquid. *Zh. Eksp. Teor. Fiz.* **19**, 105–120; also in *Collected Works of L. P. Kapitza* (ed. D. Ter Haar). Pergamon, Oxford, 1965.

Kerchman, V. I. & Frenkel, A. L. 1994 Interactions of coherent structures in a film flow: simulations of a highly nonlinear evolution equation. *Theor. Comput. Fluid Dyn.* **6**, 235–254.

Kheshgi, H. S. & Scriven, L. E. 1987 Distributed film flow on a vertical plate. *Phys. Fluids* **30**, 990–997.

Krantz, W. B. & Goren, S. L. 1971 Stability of thin liquid films flowing down a plane. *Ind. Engng Chem. Fundam.* **10**, 91–101.

Lee, J.-J. & Mei, C. C. 1996 Stationary waves on an inclined sheet of viscous fluid at high Reynolds and moderate Weber numbers. *J. Fluid Mech.* **307**, 191–229.

Liu, J. & Gollub, J. P. 1994 Solitary wave dynamics of film flows. *Phys. Fluids* **6**, 1702–1712.

Liu, J., Paul, J. D. & Gollub, J. P. 1993 Measurements of the primary instabilities of film flow. *J. Fluid Mech.* **250**, 69–101.

Liu, J., Schneider, J. B. & Gollub, J. P. 1995 Three-dimensional instabilities of film flows. *Phys. Fluids* **7**, 55–67.

Madsen, O. S. & Mei, C. C. 1969 The transformation of a solitary wave over an uneven bottom. *J. Fluid Mech.* **39**, 781–791.

Malamataris, N. T. & Papanastasiou, T. D. 1991 Unsteady free surface flows on truncated domains. *Ind. Engng Chem. Res.* **30**, 2210–2219.

Mei, C. C. 1989 *The Applied Dynamics of Ocean Surface Waves*, pp. 554–559. World Scientific.

Nakoryakov, V. E., Pokusaev, B. G. & Alekseenko, S. V. 1976 Two-dimensional roll waves on vertical falling liquid films. *Sov. J. Engng Phys.* **30**, 780.

Nguyen, L. T. & Balakotaiah, V. 2000 Modeling and experimental studies of wave evolution on free falling viscous films. *Phys. Fluids* **12**, 2236–2256.

Pearson, F. W. & Whitaker, S. 1977 Some theoretical and experimental observation of wave structure of falling liquid films. *Ind. Engng Chem. Fundam.* **16**, 401–408.

Prokopiou, T., Cheng, M. & Chang, H.-C. 1991 Long waves on inclined films at high Reynolds number. *J. Fluid Mech.* **222**, 665–691.

Salamon, T. R., Armstrong, R. C. & Brown, R. A. 1994 Traveling waves on inclined films: numerical analysis by the finite-element method. *Phys. Fluids* **6**, 2202–2220.

Shkadov, V. Ya. 1967 Wave conditions in the flow of thin layer of a viscous liquid under the action of gravity. *Izvz. Akad. Nauk. SSSR, Mekh. Zhidk i Gaza* **1**, 43–50.

Stainthorp, F. P. & Allen, J. M. 1965 The development of ripples on the surface of liquid film flowing inside a vertical tube. *Trans. Inst. Chem. Engrs* **43**, 85–91.

Trifonov, Yu. Ya. & Tsvelodub, O. Yu. 1991 Nonlinear waves on the surface of a falling liquid film. Part 1. Waves of the first family and their stability. *J. Fluid Mech.* **229**, 531–554.

Tsvelodub, O. Yu. & Trifonov, Yu. Ya. 1992 Nonlinear waves on the surface of a falling liquid film. Part 2. Bifurcations of the first-family waves and other types of nonlinear waves. *J. Fluid Mech.* **244**, 149–169.

Whitaker, S. 1964 Effect of surface active agents on stability of falling liquid films. *Ind. Engng Chem. Fundam.* **3**, 132–142.

Wilson, S. D. & Jones, A. F. 1983 The entry of a falling film into a pool and the air-entrainment problem. *J. Fluid Mech.* **128**, 219–230.

Yu, L.-Q., Wasden, F. K., Dukler, A. E. & Balakotaiah, V. 1995 Nonlinear evolution of waves on falling films at high Reynolds number. *Phys. Fluids* **7**, 1886–1902.